

DTIC FILE COPY

4

ARL-STRUC-R-428

AR-004-543

**AD-A198 343**

**DEPARTMENT OF DEFENCE**

**DEFENCE SCIENCE AND TECHNOLOGY ORGANISATION**

**AERONAUTICAL RESEARCH LABORATORIES**

**MELBOURNE, VICTORIA**

Structures Report 428

**IN-PLANE MOIRE OPTICAL PROCESSING AT ARL (U)**

DTIC  
SEP 06 1988  
D O

by

K.C. Watters

Approved for Public Release.

This work is copyright. Apart from any fair dealing for the purpose of study, research, criticism or review, as permitted under the Copyright Act, no part may be reproduced by any process without written permission. Copyright is the responsibility of the Director Publishing and Marketing, AGPS. Inquiries should be directed to the Manager, AGPS Press, Australian Government Publishing Service, GPO Box 84, Canberra, ACT 2601.

JULY 1987

88 9 6 11 F

AR-004-543

DEPARTMENT OF DEFENCE  
DEFENCE SCIENCE AND TECHNOLOGY ORGANISATION  
AERONAUTICAL RESEARCH LABORATORIES

Structures Report 428

**IN-PLANE MOIRE OPTICAL PROCESSING AT ARL (U)**

BY  
K.C. Watters

**SUMMARY**

*The principle and operation of the ARL in-plane moire optical processor are described in detail. The processor uses extensive spatial filtering to produce dual-beam interference moire fringes of high contrast. Fringe patterns obtained from a J-integral specimen and a cold-worked bolt hole specimen are shown. They compare well with displacement contour patterns obtained from a theoretical analysis and strain gauge data.*

THE UNITED STATES NATIONAL  
TECHNICAL INFORMATION SERVICE  
IS AUTHORISED TO  
REPRODUCE AND SELL THIS REPORT



© COMMONWEALTH OF AUSTRALIA 1987

---

POSTAL ADDRESS: Director, Aeronautical Research Laboratories,  
P.O. Box 4331, Melbourne, Victoria, 3001, Australia

# NOTATION

$\beta$	angular deviation normal to grating rulings
$\epsilon$	fractional pitch difference
$\epsilon_{rr}$	radial strain
$\xi$	angle to rulings of first grating
$\xi_0$	angle between moire fringe and first grating rulings
$\lambda$	wavelength of light
$\theta$	angle between rulings of two gratings or angular co-ordinate
$a$	hole radius or crack length
$p$	beam order from first grating
$q$	beam order from second grating
$r$	order of beam group from two gratings or radial co-ordinate
$s$	fringe spacing in direction $\xi$
$s_n$	fringe spacing in direction normal to fringes
$u_p$	radial displacement
$u_0$	radial displacement reference
$u_c, v_c$	Cartesian displacement components
$w$	basic grating pitch



Accession For	
NTIS CR&I	<input checked="" type="checkbox"/>
DTIC TAB	<input type="checkbox"/>
Unannounced	<input type="checkbox"/>
Justification	
B.	
Distribution	
Availability Codes	
Avail and/or	
DL	
A-1	

## CONTENTS

	Page No.
1. INTRODUCTION	1
2. BASIC MOIRE PRINCIPLE	3
3. MOIRE INTERFERENCE THEORY	3
4. THE ARL TECHNIQUE	5
5. OPTICAL PROCESSING	6
6. TEST SPECIMENS	7
7. TEST RESULTS	7
7.1 The J-integral specimen	7
7.2 The cold-worked bolt hole specimen	7
8. ANALYSIS OF RESULTS	8.
8.1 The J-integral specimen	8.
8.2 The cold-worked bolt hole specimen	8.
9. CONCLUSION	10.
10. ACKNOWLEDGMENT	10.
11. REFERENCES	11
12. TABLES	
13. FIGURES	
14. APPENDIX A	
15. DISTRIBUTION LIST	
16. DOCUMENT CONTROL DATA	

## 1. INTRODUCTION

In-plane moire is a well established full-field method for measuring the surface deformation of a specimen or component.<sup>1,2</sup> The method is generally restricted to flat surfaces, and requires a grid of lines to be attached to the surface, thereby deforming with it. Apart from these restrictions, the method is straightforward and versatile, and is being implemented at ARL as a general purpose procedure for full-field strain analysis of specimens.

The sensitivity of the in-plane moire method is related to the frequency of the grid attached to the specimen surface, and this can be varied from very coarse to very fine. Alternate methods, such as holographic interferometry and photoelastic coating, do not have this flexibility. Holographic interferometry is too sensitive for application to large deformation conditions, such as plasticity. On the other hand, photoelastic coating is too insensitive to be useful in the elastic regime. Furthermore, the in-plane moire method is readily adapted to the normal mechanical testing environment. Holographic interferometry is generally restricted to the optics laboratory, with a high level of vibration isolation.

A vast number of techniques for applying the in-plane moire method has been developed (see Reference 3 for a comprehensive review). In the early stages, grid frequencies were restricted to the order of 40 lines/mm to avoid grid diffraction effects. This rendered the method too insensitive for engineering materials, and it was mainly applied to flexible model materials.<sup>1,2</sup> Techniques such as mismatch<sup>4</sup> and fringe shifting<sup>5</sup> were devised to effectively increase sensitivity. However, the success of such techniques was limited. The next development was to apply coherent optics techniques<sup>6</sup>. This allowed higher grid frequencies to be used, without adverse diffraction effects. It also enabled optical processing, whereby the moire fringe density could be multiplied by an integral factor, up to twenty.<sup>7</sup> The limit of this development has produced sensitivities approaching those of holographic interferometry.<sup>8</sup>

Work has been progressing at ARL towards implementing the in-plane moire method. The chosen technique consists of photographing a deformed specimen grid, producing a moire fringe pattern from that photograph in a coherent optical processor, and automatically analysing that fringe pattern using a TV camera interfaced with a computer. At this stage the apparatus and procedures for grid photography and optical processing have been developed and are described in this report.

The optical processor has been designed to produce pure dual-beam interference moire fringes of high contrast. The processor gives a fringe multiplication effect of two. So far, only coarse grids have been used (40 lines/mm). Grid frequencies may be increased in the future as the system finds wider application. However, extremely fine grids will not be required because the automatic analysis system will acquire data at regular intervals between fringes, rather than just at fringe centrelines. The system sensitivity will be limited more by the spatial resolution of the TV camera than by the grid frequency.

A companion report to this one has been written<sup>9</sup>, describing in detail the techniques used for grid application, grid photography, and optical processing to produce moire fringe patterns. This report concentrates on the theory behind the optical processor and presents some quantitative results obtained from specimens.

## 2. BASIC MOIRE PRINCIPLE

A moire fringe pattern is formed when two similar gratings are superimposed. A grating consists of a fine set of parallel lines or furrows on a surface. Obviously, at least one of the surfaces must be transparent for the fringe pattern to be observable.

The moire fringes arise from any slight difference in pitch (line spacing) between the gratings, or from any slight relative rotation of the gratings. These can be global effects, when one grating has a slightly different nominal pitch to the other, or when one grating has a slight rigid body rotation relative to the other. In such cases the moire fringes will be equally spaced parallel straight lines. Alternatively, there can be local pitch differences or relative rotations between the gratings, if one is nominally identical to the other but has suffered some distortion. In this case the moire fringes form a contour pattern of the distortion, providing no global fringes are present.

This principle is utilised in the in-plane moire method. One grating is attached to the surface of a specimen and deforms as the specimen surface deforms. The other grating remains undeformed and serves as a reference. The moire fringes are contours of the in-plane displacement of the specimen surface in the direction perpendicular to the reference grating lines. Normally, a grid of orthogonal parallel lines is attached to the surface of the specimen, rather than a unidirectional grating. This allows fringe patterns for two orthogonal in-plane displacement components to be obtained separately, using two orientations of the reference grating.

## 3. MOIRE INTERFERENCE THEORY

The formation of moire fringes from superposed gratings can be explained, using geometric optics principles, as a blockage or vernier effect.<sup>2</sup>

This explanation is valid for ronchi amplitude gratings (dark or opaque lines on a light or transparent background) of low frequency (frequency = 1/pitch). However, for phase gratings (regular furrows on the surface), or at high frequencies where diffraction becomes significant, moire fringes are interpreted, using wave optics principles, as interference fringes between slightly non-parallel coherent light beams.

Reference 10 is a comprehensive presentation of the interference theory of the formation of moire fringes. A summary of that theory, with relevance to the ARL optical processor, is presented here.

Consider a transparent grating of pitch  $w$ , illuminated normal to its surface by a collimated beam of coherent monochromatic light of wavelength  $\lambda$ . An interference pattern is generated by the grating on its exit side, such that virtually all the transmitted light energy is confined in a series of very narrow angular bands in orientations defined by:

$$\sin \beta_p = \frac{p\lambda}{w} \quad p, = 0, \pm 1, \pm 2, \dots \quad (1)$$

The angular deviation  $\beta_p$  is in the direction normal to the grating rulings (lines or furrows). There is no deviation in the direction parallel to the grating rulings (see Figure 1). This is classic diffraction grating action, and a full presentation can be found in any standard physics text book such as Reference 11.

Now consider two such gratings in series. The emergent beams from the first grating become the incident beams for the second grating. Suppose the surfaces of the two gratings are parallel and separated by a small air gap. Furthermore, suppose that the rulings of the two gratings make a small angle  $\theta$  with each other and that their pitches are slightly different. Let the pitch of the first grating be  $w$  and that of the second grating be  $w(1 + \epsilon)$ .

Consider the  $p$ th beam from the first grating. It will be broken up by the second grating into a number of beams with angular deviations given by an equation similar to Equation 1. For the  $q$ th of these beams, the angular deviation in the direction normal to the first gratings' rulings, as derived in Appendix A, is given by:

$$\sin \beta_{pq} = \lambda \{ p\epsilon + (p + q \cos \theta) \} / \{ w(1 + \epsilon) \}. \quad (2)$$

The intergrating angle  $\theta$  also causes a small deviation in the direction parallel to the first grating's rulings, but this can be ignored for the purpose of this discussion.

If the two gratings' rulings had the same orientation and pitch ( $\theta = \epsilon = 0$ ), Equation 2 would reduce to:

$$\sin \beta_{pq} = \lambda(p + q) / w. \quad (3)$$

In this case, any emergent beams from the second grating with order sequences  $p, q$  adding up to the same value ( $p + q = r$ ) will be parallel. Thus the emergent beams from the second grating can be conveniently grouped into sets of parallel beams. These are called  $r$ -groups. When the two gratings' rulings have slightly different orientations and pitches ( $\theta, \epsilon \neq 0$ ), the beams in an  $r$ -group are no longer precisely parallel. However, their deviation from parallelism is small compared to the angular deviation between groups, and the  $r$ -group concept is still valid.

The small angular separation between the member beams of an  $r$ -group produces interference fringes — the moire fringes. An  $r$ -group contains member beams with order sequences like  $p, r - p$ . Consider two member beams with order sequences  $p_1, r - p_1$  and  $p_2, r - p_2$ . It can be shown from Equation 2 that the angular separation between these beams is directly proportional to  $p_1 - p_2$ . The density of fringes from interfering beams is directly proportional to their angular separation. Therefore, adjacent members in an  $r$ -group ( $p_1 - p_2 = 1$ ) interfere to produce a fringe pattern with some fundamental density, while more widely separated members, e.g.  $p_1 - p_2 = m$ , interfere to produce a fringe pattern with  $m$  times that fundamental density. The relation between the fundamental fringe density and the grating parameters will be presented later.

For any  $r$ -group the nature of the moire fringe pattern depends on the relative phases and amplitudes of the member beams. These in turn depend on the ruling characteristics of the two gratings and the  $r$ -group under consideration. If an  $r$ -group contains a number of beams of even intensity, multi-beam interference will result and the moire fringe pattern will take the form of narrow primary maxima or minima with the fundamental spacing, and numerous indistinguishable secondary maxima and minima between them. If an  $r$ -group contains two dominant beams with order sequences  $p_1, r - p_1$  and  $p_2, r - p_2$ , the moire fringe pattern will have a sinusoidal intensity distribution with fringe spacing  $1/|p_1 - p_2|$  times the fundamental spacing. Thus, controlling the dominant beams by suitably blazing the gratings is a means to achieve fringe multiplication. Also, spatial filtering can be used to control the constituent beams of an  $r$ -group and hence the spacing and intensity profile of the moire fringe pattern.

A geometric argument is presented in Reference 10 to show that, if the first grating is traversed at an angle  $\xi$  to its rulings, and the fractional location within the rulings of the first grating is monitored with respect to the fractional location of the normal projection of the traverse point within the rulings of the second grating, then conditions repeat at intervals given by:

$$s = w(1 + \epsilon) \{ (1 + \epsilon - \cos \theta) \sin \xi + \sin \theta \cos \xi \}^{-1}. \quad (4)$$

Conditions are constant in directions for which  $s$  is infinite, i.e.  $\xi = \xi_0$  with  $\xi_0$  given by:

$$(1 + \epsilon - \cos \theta) \sin \xi_0 + \sin \theta \cos \xi_0 = 0, \quad (5)$$

from which

$$\tan \xi_0 = -\sin \theta / (1 + \epsilon - \cos \theta).$$

The repeat interval in the direction normal to  $\xi_0$  is found by substituting  $\xi = \xi_0 \pm \pi/2$  into Equation 4. This results in:

$$s_0 = w(1 + \epsilon) [\epsilon^2 + 2(1 + \epsilon)(1 - \cos \theta)]^{1/2}. \quad (6)$$

Directions in which relative conditions between the gratings are constant are also directions in which emergent light intensity will be constant. Therefore Equation 5 defines the orientation of the moire fringes. The repeat interval normal to this direction defines the minimum distance to be traversed before the emergent light intensity returns to its current value. This is the fundamental moire fringe spacing and it is given by Equation 6. The fundamental fringe density is  $1/s_0$ .

It has been shown in the preceding paragraph that the direction and spacing of the moire fringes can be related to the expansion and rotation of one grating relative to the other. However, a more useful interpretation of moire fringes can be made. The second grating, which is expanded and rotated relative to the first, can be considered to have initially been identical to the first grating, and then deformed. If relative conditions between the two gratings repeat, then the second grating must have moved in the direction normal to the rulings of the first grating by one pitch of the first grating during the repeat interval (see Figure 2). The moire fringes can then be interpreted as contours of displacement of a deformed grating relative to a reference grating in the direction normal to the reference grating rulings. The displacement interval between fringes with the fundamental spacing is equal to the pitch of the reference grating.

So far, consideration has been confined to the case of the second grating being uniformly expanded and rotated relative to the first. However, the arguments are equally valid in the non-uniform case when applied to a small area of the second grating in which conditions may be taken as uniform. Therefore Equations 4 to 6 have local validity in the non-uniform case as well as global validity in the uniform case. Also, the interpretation of moire fringes as displacement contours is valid for the non-uniform case. Continuity of displacement ensures smooth continuity of the moire fringes in the non-uniform case, despite changes in fringe orientation and spacing.

The orientation and fundamental spacing of the fringes, has been defined and qualitative examination of intensity distributions in relation to r-group constituents has been made. However, the location of the fringes has not been defined. Normally the location of the fringe pattern does not matter. Without it the pattern has no zero reference, but relative displacement and strain data can be obtained. Nonetheless, it is useful to consider the factors affecting fringe pattern location. The fringe pattern could be located if the transmitted light intensity could be defined at any particular point. However, the intensity definition at any particular point is currently an unsolvable problem. It is influenced by such parameters as the ruling characteristics of the gratings, the r-group under consideration, the gap between the gratings, and the location of the first ruling of one grating relative to that of the other. The latter two of these parameters are of interest. Changing the relative locations of the first rulings of the gratings provides a means to globally shift the fringe pattern. This technique will be used in future as part of a calibration procedure for automatic fringe analysis. A movement of one grating pitch of the reference grating will reproduce the initial fringe pattern. The intergrating gap effect is of interest because of its possible detrimental influence on the fringe pattern. If the gratings are flat and parallel, changing the gap only causes global shifting of the fringe pattern. However, if the gratings are not precisely flat and parallel, local zero shifts of the fringe pattern will be present. This would appear as distortions of the fringe pattern and degrade the accuracy of the fringes as a measure of in-plane displacement. This point will be discussed later in relation to the ARL optical processor.

#### 4. THE ARL TECHNIQUE

A brief description of the ARL in-plane moire technique is given here. For a more detailed description see Reference 9.

The first step is to apply a grid of lines to the surface of the specimen. The surface is first polished and then coated with photoresist (a photographic emulsion). The photoresist coating is applied by either a spinning or a spray technique. All grids and gratings used in the ARL technique are of ronchi type with dark or opaque lines on a light or transparent background, and unit line width to space ratio. A master grid is placed against the coated specimen surface and the photoresist is exposed by a mercury arc lamp. The photoresist is then developed.

The next step is to photograph the specimen grid after it has been deformed. In ARL tests the deformed state of the specimen occurs from such processes as cold working, particularly around a bolt hole, or holding the specimen under load in a testing machine. For photography, the deformed specimen surface is illuminated by short duration, high power flashlights, so specimen vibration is not a problem. A De Vere plate camera is used, fitted with a Schneider symmar lens. The camera is set up to give accurate one-to-one photography of the specimen surface using Kodak Technical Pan film.

The photograph of the deformed specimen grid is then placed in the optical processor to produce a moire fringe pattern. The optical processor is described in the next section. The fringe pattern is photographed with a 35 mm camera. In the future the fringe pattern will be captured by a TV camera for automatic fringe analysis.



## 5. OPTICAL PROCESSING

Figure 3 is a schematic diagram of the ARL moire optical processor. It is based on a hybrid image processor developed by CSIRO.<sup>12</sup> A full description of the optical components of the processor is given in Reference 9.

A collimated monochromatic light beam ( $\lambda = 546 \text{ nm}$ ) is produced from a mercury arc lamp by passing its output through a narrow band filter, a spatial filter and a collimator. The beam then passes through the specimen grid photograph which is located at the front focal plane of a Fourier transform lens. In the back focal plane of the Fourier transform lens the image from the specimen grid is spatially filtered. The light transmitted by the filter then passes through a second Fourier transform lens which creates a filtered image of the specimen grid in its back focal plane. The reference grating is also located in this plane and the moire fringe pattern is generated there. The transmitted light from the reference grating is focused and spatially filtered before final photography of the moire fringe pattern.

The specimen grid photograph acts as a diffraction grating in two directions. The discrete beams formed by the specimen grid photograph are focused by the Fourier transform lens as a two-dimensional array of spots in its back focal plane. Figure 4 is a schematic diagram of the array of spots, while Figure 5 is a photograph of the array from a typical specimen grid photograph. The general halo of light in Figure 5 results from back reflections from uncoated lens surfaces. The focused array of spots produced by a grating can be interpreted<sup>13</sup> as a Fourier transform of the grating transmission. The Fourier transform of a ronchi grid with unit line width to space ratio has no even orders, i.e. the possible orders are  $p = 0, \pm 1, \pm 3, \dots$  in two dimensions. This is demonstrated in Figures 4 and 5. The spatial filter in the transform plane allows only the  $\pm 1$  order spots in the vertical or horizontal direction to pass through. Referring to Figure 4, spots  $-1, 0$  and  $+1, 0$  are transmitted by the spatial filter in order to obtain a fringe pattern for the horizontal displacement component. Because the transmitted spots have no vertical separation, the horizontal lines of the specimen grid photograph are eliminated by the filtering.<sup>13</sup> The image created by the second Fourier transform lens is then a grating with vertical rulings. The reference grating is also oriented with its rulings vertical. Conversely, in order to obtain a fringe pattern for the vertical displacement component, spots  $0, -1$  and  $0, +1$  of Figure 4 are transmitted by the spatial filter, and the reference grating is oriented with its rulings horizontal.

The  $\pm 1$  order beams from the specimen grid photograph each divide into a further number of beams upon transmission through the reference grating. The reference grating is ronchi type with the same frequency as the specimen grid photograph. The order sequences of the member beams of the resulting  $r$ -groups are given in Table 1. No odd  $r$ -groups are present except for  $r = \pm 1$ . These two groups each contain only one beam, and so no moire fringes. The  $r$ -groups are brought to a focus behind the reference grating where a spatial filter allows only the group  $r = 0$  to pass. This group contains two beams with order sequences  $+1, -1$  and  $-1, +1$ . The optical processor has a fringe multiplication effect of two, because the difference in order between the  $+1$  and  $-1$  beams filtered from the specimen grid photograph is 2.

The moire optical processor has a number of good features. Because of symmetry, the two beams in the  $r = 0$  group are of equal intensity and interfere to produce maximum contrast fringes with a sinusoidal intensity profile. This is a requirement for automatic fringe analysis. The Fourier filtering and imaging section of the processor (see Figure 3) superimposes a filtered image of the specimen grid photograph on the reference grating, so there is effectively little or no gap between the gratings. However, any detrimental effect of a gap between the gratings (see Section 3) is eliminated by the overall symmetry of the processor. In Reference 14 it is shown that the moire fringe pattern is insensitive to the intergrating gap when the angle of incidence to the first grating equals the deviation angle of the  $r$ -group under consideration from the second grating — the condition of minimum deviation.<sup>10</sup> The normal incidence and observation angles of the ARL processor satisfy this condition. Finally, the section of the processor comprising the specimen grid photograph, the Fourier transform lenses and the reference grating, forms a telecentric arrangement.<sup>15</sup> A feature of such an arrangement is that it produces an image of the specimen grid photograph on the reference grating with unit magnification,<sup>15</sup> insensitive to precise location of the specimen grid photograph.

## 6 TEST SPECIMENS

The ARL in-plane moire technique has been demonstrated on two specimen types. The first was a J-integral specimen and the second was a cold-worked bolt hole specimen. One of each specimen type was tested.

Figure 6 shows the geometry of the J-integral specimen. It was made of 7010-T73651 aluminium alloy. A fatigue crack was grown in the specimen at the base of the notch to an overall length of 25.16 mm by cyclic tensile loading through the bolt holes. A grid of lines of frequency 40 lines/mm was then applied to one face of the specimen around the notch and crack.

The geometry of the cold-worked bolt hole specimen is shown in Figure 7. It was made of 2024-T4 aluminium alloy. Grids of lines of frequency 20 lines/mm were applied to the front and back faces of the specimen around the central hole.

## 7. TEST RESULTS

### 7.1 The J-integral specimen

A Hounsfield Tensometer was used to apply tensile load to the J-integral specimen through the bolt holes. Load was increased monotonically to 3.17 kN and then released. Photographs of the gridded surface of the specimen were taken at load levels 0, 1.06 kN, 2.11 kN, 3.17 kN, 0. The moire fringe patterns obtained from those photographs are shown in Figures 8, 9, 10, 11 and 12.

### 7.2 The cold-worked bolt hole specimen

This specimen was gripped in an MTS servo-hydraulic mechanical testing machine for cold working in situ followed by tensile loading. The Fatigue Technology Incorporated split-sleeve process was used to cold work the central hole in the specimen. The process involved a maximum interference level of 4.2% before the mandrel was withdrawn. A hand screwed device was used to draw the mandrel through the split-sleeve lined hole in the specimen. This allowed photographs to be taken of the grid on the front face of the specimen at intermediate stages of the cold working process. Figure 13 shows the fringe patterns obtained from the photograph of the specimen when the mandrel was at the stage of producing maximum expansion of the hole. In Figure 13, and in all subsequent photographs of the cold-worked bolt hole specimen in this report, the long axis of the specimen is oriented vertically as it was in the actual test. The split in the cold working sleeve was located at the top of the hole in the figures. The missing segment of the fringe patterns in Figure 13 was caused by the shadow of the protruding mandrel from the oblique lighting. Figures 14 and 15 show the fringe patterns from the front and back faces of the specimen respectively at the completion of cold working when the mandrel and split sleeve had been removed from the hole. Photography of the back face of the specimen was performed by rotating the specimen while still gripped in the testing machine. Such rotation was enabled by the circular screwed ends of the grips, and the overall symmetry of the specimen and the grips ensured that the positions of the front and back faces were precisely interchanged upon rotation. The circular abrasion marks on the back face of the specimen evident in Figure 15 were caused by the cold working device. Figures 16 and 17 show the fringe patterns from the front and back faces of the specimen respectively when a tensile load of 47.8 kN was applied to it subsequent to the cold working. The fringe patterns after the tensile load was removed are shown in Figures 18 and 19 for the front and back faces of the specimen respectively.

## 8. ANALYSIS OF RESULTS

The in-plane moire technique described in this report uses only a coarse grid on the specimen and relies on the fringe interpolation capability of the proposed automatic fringe analysis system to achieve measurement sensitivity. Until that analysis system is functional, only crude manual processing using the fringe centreline contours could be done. In view of the coarseness of the grids, it is not considered worthwhile to perform such a manual analysis on the fringe data presented in this report. Instead, the fringe data will be superficially compared to independent theoretical and experimental data.

### 8.1 The J-integral specimen

A finite element (FE) analysis of the J-integral specimen of this report was presented in Reference 16. The mesh used in that analysis is shown in Figure 20. Quarter-point isoparametric elements were used around the crack tip and the analysis was linear elastic. Displacement contours have been obtained from output of the Reference 16 analysis, and are shown in Figures 21 and 22 for the horizontal and vertical displacement components respectively. These displacement contours are for a load of 3.17 kN and so are directly comparable to the fringe patterns of Figure 11. Only the contours in the notch root and crack region are shown in Figures 21 and 22 but this region of the mesh corresponds closely with the region to the left of the crack in the photographs of Figure 11. Comparison of Figure 21 with Figure 11(a) shows reasonable agreement between the horizontal displacement contours and the corresponding moire fringe pattern. The fringes/contours are of similar shape and orientation although the moire pattern seems to have a slightly higher fringe density. This discrepancy is attributable to the lack of symmetry in the moire fringe pattern of Figure 11(a) and the initial zero load fringe pattern of Figure 8(a). Neither problem is serious. The lack of symmetry is a result of slight rotational mismatch between the specimen and reference gratings and will be eliminated in future by better experimental technique. An initial fringe pattern can be subtracted from a final fringe pattern when the automatic fringe analysis method is implemented. The agreement between the vertical displacement contour pattern of Figure 22 and the corresponding moire fringe pattern of Figure 11(b) is better. This time the fringe pattern is symmetric, but again the zero load fringe pattern of Figure 8(b) has caused a slightly higher fringe density than the contours. The fringe adjacent to the crack in Figure 11(b) is of interest. It is distorted at the crack tip which is not reflected in the corresponding contour of Figure 22. It is likely that the distortion results from plasticity at the crack tip and the linear elastic FE analysis could not represent that zone adequately.

### 8.2 The cold-worked bolt hole specimen

In Reference 17 some strain gauge data are presented from a cold-worked bolt hole specimen. Those data are reproduced in Figure 23. The specimen used in Reference 17 was approximately double the size of the specimen of this report, but other parameters, such as shape, material, and maximum cold work interference level, were quite similar. These parameters are compared in Table 2.

The radial strain data in Figure 23 have been graphically integrated to obtain radial displacement,  $u_p$ , for the two cases of mandrel giving maximum expansion and after cold working.

$$u_p = u_o + \int_{r_o}^r \epsilon_{rr} dr$$
$$u_p/a = u_o/a + \int_{r_o/a}^{r/a} \epsilon_{rr} d(r/a)$$

where  $\epsilon_{rr}$  is the radial strain,

$r$  is the radial distance from the hole centre,

and  $a$  is the hole radius.

The cold working process in Reference 17 is axisymmetric in the vicinity of the hole and so  $\epsilon_{rr}$  and  $u_r$  are independent of angular location,  $\theta$ , and tangential displacement  $v_\theta$  is zero everywhere. The data in Figure 23 lie between  $r/a = 1.125$  and  $r/a = 2.25$ . The radial displacement data relative to  $u = u_0$  at  $r_0/a = 1.125$  are then as given in Tables 3 and 4. Empirical functions have been fitted through those data of the form:

$$r/a = f(u_r/a - u_0/a)$$

A transformation to cartesian coordinates was effected as:

$$u_r/a = (u_p/a) \cos \theta$$

$$v_\theta/a = (u_p/a) \sin \theta$$

Contour points ( $r/a$ ,  $\theta$ ) of  $u_r/a$  and  $v_\theta/a$  can be established by selecting a contour level and then selecting a range of values for  $\theta$ . For each contour level and  $\theta$  value, a value can be calculated for  $u_p/a$ , and in turn a value for  $r/a$ . If  $1.125 \leq r/a \leq 2.25$ , the contour point falls within the data range and is acceptable.

The contour interval of the moire fringe patterns of Figures 13 and 14 is 0.025 mm. Referring to Figures 13(a) and 14(a) for the horizontal displacement component, the fringes starting at the bottom of the hole can be taken as zero order. Then a fringe from the left side of the hole can be used to set the radial displacement reference  $u_r/a$ . This is done by selecting a fringe and determining its order by fringe counting from the zero order fringe. The radial displacement  $u_r$  of this fringe is then the fringe order multiplied by the contour interval. The normalised radial location  $r/a$  of the fringe gives the relative displacement  $u_r/a - u_0/a$  by interpolating data in Table 3 or 4. Then  $u_r/a$  is found by subtracting  $u_p/a - u_0/a$  from  $u_p/a$ . The values so obtained for  $u_r/a$  are 0.0273 and 0.0205 for the cases of maximum expansion and after cold working respectively.

Using the above procedure, normalised displacement contours were established with a normalised contour interval of  $0.025/4.185 = 0.005974$  to correspond with the moire fringe patterns. The contour plots are shown in Figure 24 for the case of the mandrel giving maximum expansion and in Figure 25 for the case of after cold working. The plots in Figures 24 and 25 have been made round only half the hole circumference. Symmetric contours would apply to the other half. The contours have been truncated at the limiting  $r/a$  values of the data in Figure 23. The contours in Figures 24 and 25 are directly comparable to the fringes around the lower half of the hole in Figures 13 and 14 respectively. It is not appropriate to compare the contour plots to the fringe patterns round the upper half of the hole because the split in the sleeve of the cold working procedure used for this report causes a severe local distortion of the fringes.

Correspondence between the contour plots of Figures 24 and 25 and the moire fringe patterns of Figures 13 and 14 is very good. Any slight differences may be attributable to the different cold-working procedure, the slightly lower yield stress and the slightly higher cold work interference level of the specimen in Reference 16 (see Table 2).

It is of interest to compare the fringe patterns of Figures 14 and 15 before loading with those of Figures 18 and 19 after loading. Qualitative inspection shows no discernible difference between Figures 14 and 15 and Figures 18 and 19 respectively. Yet, the intervening loading to 47.8 kN (see Figures 16 and 17) was sufficient to cause yielding around the hole if it had not been cold worked. Using a stress concentration factor of 3.0, an elastic analysis of the specimen with no residual stresses gives a maximum stress at the side of the hole of 635.6 MPa at 47.8 kN. This is well in excess of the yield stress of 380 MPa (see Table 2). Obviously, the residual compressive stresses from cold working the hole offset the elastic tensile stress concentration sufficiently to prevent yielding. This is a graphic demonstration of the benefit of cold working.

## **9. CONCLUSION**

The theory and operation of the ARL moire optical processor have been presented in this report. Results obtained from two test specimens have also been presented. The fringe patterns in Figures 8 to 19 demonstrate that the ARL moire processor can produce good quality, high contrast fringes. With on-going refinement of experimental apparatus and techniques, such fringe patterns should be well suited to automatic data processing. The validity of the moire fringes as specimen displacement contours has been verified by comparing them to independently obtained displacement contours. The benefit of cold working bolt holes in offsetting the effect of elastic tensile stress concentration was clearly demonstrated by the fringe patterns of the report.

### **Acknowledgment**

The author wishes to acknowledge the effort of Mr B. Lawrie of Structures Division, ARL in performing all the experimental work of this report.

### References

1. Theocaris P., Moire fringes in strain analysis, London: Pergamon Press, 1969.
2. Durelli A.J. and Parks V., Moire analysis of strain, Englewood Cliffs, N.J.: Prentice-Hall Inc., 1970.
3. Sciammarella C.A., The moire method — a review, *Experimental Mechanics*, vol. 22, no. 11, Nov. 1982, pp 418-433.
4. Chiang F.P., Moire methods of strain analysis, from *Manual on experimental stress analysis*, third edition, Wesport, CT: Society for Experimental Stress Analysis, 1978.
5. Chiang F.P., Parks V.J. and Durelli A.J., Moire-fringe interpolation and multiplication by fringe shifting, *Experimental Mechanics*, vol. 8, no. 12, Dec. 1968, pp 554-560.
6. Post D., New optical methods of moire fringe multiplication, *Experimental Mechanics*, vol. 8, no. 2, Feb. 1968, pp 63-68.
7. Post D. and MacLaughlin T.F., Strain analysis by moire-fringe multiplication, *Experimental Mechanics*, vol. 11, no. 9, Sep. 1971, pp 408-413.
8. Post D., Moire interferometry at VPI&SU, *Experimental Mechanics*, vol. 23, no. 6, June 1983, pp 203-210.
9. D'Cruz J., Lawrie B.L., Watters K.C. and Rumble S.J., Experimental aspects of in-plane displacement measurement using a moire fringe technique, *Aust. Aeronaut. Res. Lab. Struct. Tech. Memo. 440*, June 1986.
10. Guild J., *The interference systems of crossed diffraction gratings*, Oxford:Clarendon Press, 1956.
11. Halliday D. and Resnick R., *Physics*, Wiley International Combined edition, Tokyo:Toppan Co. Ltd., 1966.
12. Hariharan P., Oreb B.F. and Brown N., A simple hybrid image processor, *Journal of Electrical and Electronics Engineering, Australia*, Vol. 3, No. 4, Dec. 1983.
13. Cloud G.L., Simple optical processing of moire grating photographs, *Experimental Mechanics*, vol. 20, no. 8, Aug. 1980, pp 265-272.
14. Post D., Moire fringe multiplication with a nonsymmetrical doubly blazed reference grating, *Applied Optics*, vol. 10, no. 4, April 1971, pp 901-907.
15. Holister G.S. and Watts D., Telecentric systems for moire analysis, *Experimental Mechanics*, vol. 10, no. 1, Jan. 1970, pp 31-38.
16. Beaver P.W., Heller M. and Rose T.V., Experimental and theoretical determination of  $J_{IC}$  for 2024-T351 aluminium alloy, *Aust. Aeronaut. Res. Lab. Struct. Rep. 420*, July 1986.
17. Lowak H., Zum einfluss von bauteilgrobe, lastfolge und lasthorizont auf die schwingfestigkeitssteigerung durch mechanisch erzeugte druckeigenspannungen, *Fraunhofer — Institut für Betriebsfestigkeit Darmstadt, Bericht Nr. FB-157*, 1981.

Table 1

The low order r-groups from the ARL moire optical processor

r-group	Order sequences of member beams	
4	+1, +3	-1, +5
3		
2	+1, +1	-1, +3
1	+1, 0	
0	+1, -1	-1, +1
-1		-1, 0
-2	+1, -3	-1, -1
-3		
-4	+1, -5	-1, -3

Table 2

Comparison of cold-worked bolt hole specimens

Parameter	Reference 16 specimen	Specimen of this report
Hole diameter (mm)	16	8.37
Width (mm)	80	44.5
Thickness (mm)	10	5.07
Width/hole diameter	5.0	5.3
Thickness/hole diameter	0.63	0.61
Material	2024	2024-T4
Yield stress (MPa)	350	380
Cold work interference level	4.5%	4.2%

Table 3

Radial displacement with mandrel giving maximum expansion

$r/a_1$	1.125	1.25	1.375	1.5	1.625
$u_p/a_1$	0	-0.0043	-0.0074	-0.0099	-0.0119
$r/a_1$	1.75	1.875	2.0	2.125	2.25
$u_p/a_1$	-0.0136	-0.0149	-0.0159	-0.0166	-0.0172

Table 4

Radial displacement after cold working

$r/a_1$	1.125	1.25	1.375	1.5	1.625
$u_p/a_1$	0	-0.0037	-0.0063	-0.0083	-0.0098
$r/a_1$	1.75	1.875	2.0	2.125	2.25
$u_p/a_1$	-0.0110	-0.0119	-0.0126	-0.0130	-0.0133

## APPENDIX A

### Beam Deflection from Two Gratings in Series

The action of two gratings in series on a transmitted beam of light is shown in Figure A1 by tracing the path of one ray from one beam order sequence. The surfaces of the two gratings are parallel, with gap  $g$ . The rulings of the second grating make an angle  $\theta$  with those of the first grating. Coordinate systems set up in the two gratings have the X axis in the plane of the grating, normal to the rulings, the Y axis parallel to the rulings and the Z axis normal to the plane of the grating.

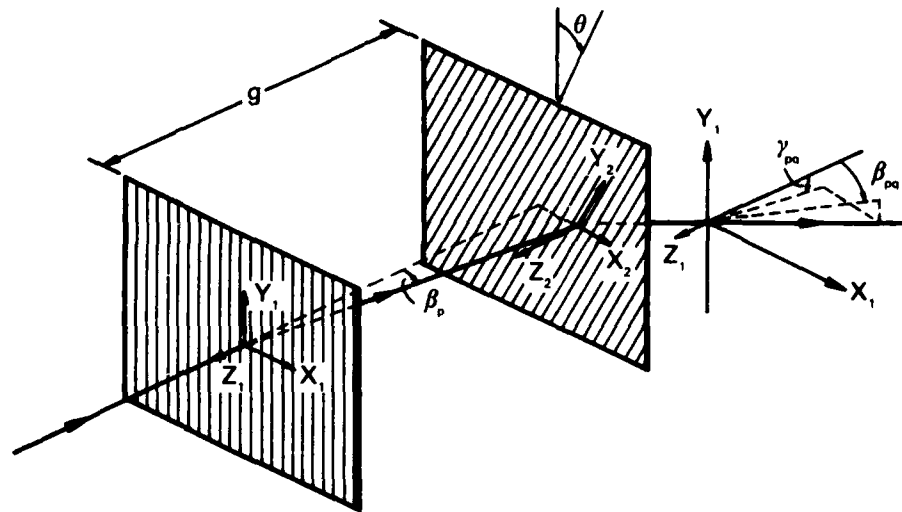


FIG A1: RAY DEFLECTIONS FROM GRATINGS IN SERIES

Figure A2 shows the relative orientations of the coordinate systems of the two gratings.

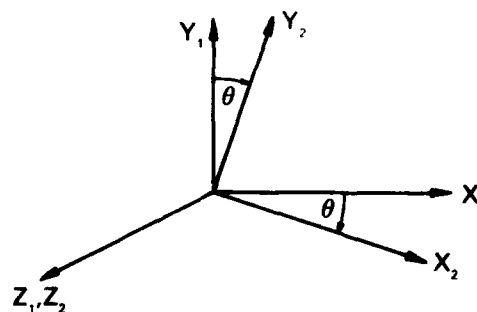


FIG A2: GRATING COORDINATE SYSTEMS



If we consider unit vectors  $i, j, k$  in the grating coordinate systems, the relation between the systems can be expressed as:

$$\begin{aligned} i_2 &= i_1 \cos \theta - j_1 \sin \theta, \\ j_2 &= i_1 \sin \theta + j_1 \cos \theta, \end{aligned} \quad (A1)$$

and

$$\begin{aligned} k_2 &= k_1, \\ i_1 &= i_2 \cos \theta + j_2 \sin \theta, \\ j_1 &= -i_2 \sin \theta + j_2 \cos \theta, \\ k_1 &= k_2. \end{aligned} \quad (A2)$$

A collimated beam of light normal to the first grating has rays which can be represented as vectors  $-k_1$ . The deviation suffered by the  $p$ th order beam from the first grating, in the direction normal to the rulings of the first grating is an angle  $\beta_p$ . This is given by the classical diffraction grating formula as:

$$\sin \beta_p = \frac{p\lambda}{w}, \quad (A3)$$

where  $\lambda$  is the wavelength of the light and  $w$  is the ruling pitch of the first grating. A ray in the  $p$ th order beam transmitted by the first grating will have the vector representation  $i_1 \sin \beta_p - k_1 \cos \beta_p$ . Using Equations A2 this representation can be transformed to  $\cos \theta \sin \beta_p i_2 + \sin \theta \sin \beta_p j_2 - \cos \beta_p k_2$  relative to the reference frame of the second grating. The deviation suffered by the  $q$ th beam from this light beam vector on transmission through the second grating is slightly more complex than that given by Equation A3. The more general form of the grating equation (A3) is given in Reference 10 as:

$$\sin \alpha_t = \sin \alpha_i, \quad (A4)$$

$$\sin \beta_t = \sin \beta_i + \frac{q\lambda}{w},$$

where  $\alpha_i$  and  $\alpha_t$  are the incidence and transmission angles relative to the principal plane of the grating (the XZ plane in our reference system), and  $\beta_i$  and  $\beta_t$  are the incidence and transmission angles relative to the secondary plane of the grating (the YZ plane in our reference system). Angles  $\alpha_i$  and  $\beta_i$  are readily obtained from the components of the incident light vector as:

$$\begin{aligned} \sin \alpha_i &= \sin \theta \sin \beta_p, \\ \sin \beta_i &= \cos \theta \sin \beta_p. \end{aligned} \quad (A5)$$

Now, in substituting into Equations A4, the grating pitch  $w(1 + \epsilon)$  will be used instead of  $w$ , to give a small pitch difference between the first and second gratings. We get:

$$\sin \alpha_1 = \sin \theta \sin \beta_p \quad (A6)$$

$$\sin \beta_1 = \cos \theta \sin \beta_p + \frac{q\lambda}{w(1+\epsilon)}$$

Angles  $\alpha_1$  and  $\beta_1$  define the transmission vector from the second grating. That vector takes the form:

$$\hat{i} = \sin \beta_1 i_2 + \sin \alpha_1 j_2 - f k_2 \quad (A7)$$

where

$$f = \{1 - \sin^2 \beta_1 - \sin^2 \alpha_1\}^{1/2}$$

using the transformation equations (A1),  $\hat{i}$  is represented in the reference frame of the first grating as:

$$\begin{aligned} \hat{i} &= \sin \beta_1 (i_1 \cos \theta - j_1 \sin \theta) + \sin \alpha_1 (i_1 \sin \theta + j_1 \cos \theta) - f k_1 \\ &= (\sin \beta_1 \cos \theta + \sin \alpha_1 \sin \theta) i_1 + (\sin \alpha_1 \cos \theta - \sin \beta_1 \sin \theta) j_1 - f k_1 \end{aligned} \quad (A8)$$

From the transmission vector of Equation A8, the transmission angle  $\alpha_{pq}$  and  $\beta_{pq}$  relative to the principle and secondary planes respectively ( $X_1Z_1$  and  $Y_1Z_1$ ) of the first grating are given by:

$$\sin \alpha_{pq} = \sin \alpha_1 \cos \theta - \sin \beta_1 \sin \theta \quad (A9)$$

$$\sin \beta_{pq} = \sin \alpha_1 \sin \theta + \sin \beta_1 \cos \theta$$

Substituting for  $\alpha_1$  and  $\beta_1$  from Equations A6 into Equations A9 gives:

$$\sin \alpha_{pq} = -\frac{q\lambda}{w(1+\epsilon)} \sin \theta \quad (A10)$$

$$\sin \beta_{pq} = \sin \beta_p + \frac{q\lambda}{w(1+\epsilon)} \cos \theta \quad (A11)$$

Substituting for  $\beta_p$  from Equation A3 into Equation A11 gives:

$$\begin{aligned} \sin \beta_{pq} &= \frac{p\lambda}{w} + \frac{q\lambda}{w(1+\epsilon)} \cos \theta \\ &= \lambda \{p\epsilon + (p + q \cos \theta) / (w(1+\epsilon))\} \end{aligned} \quad (A12)$$

Equations A10 and A12 give the deflections of a beam with order sequence  $p, q$  after transmission through two parallel gratings in series. The beam was incident normally to the first grating.

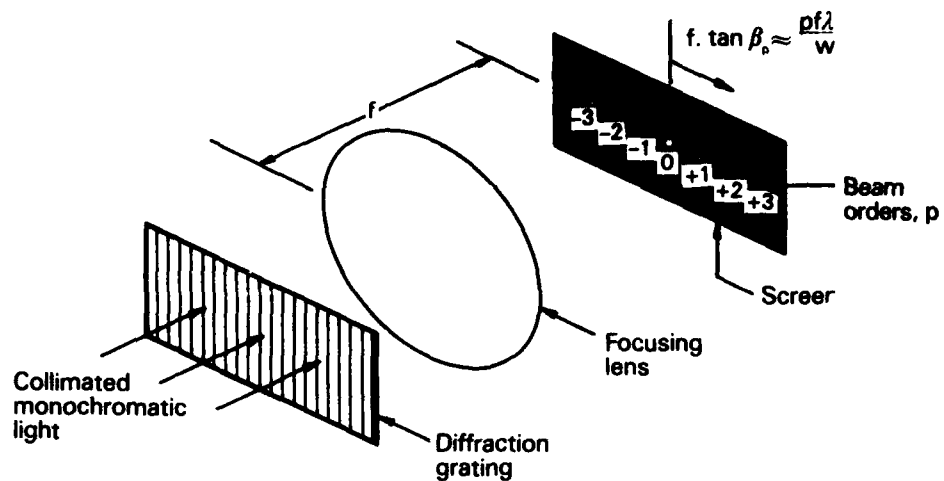
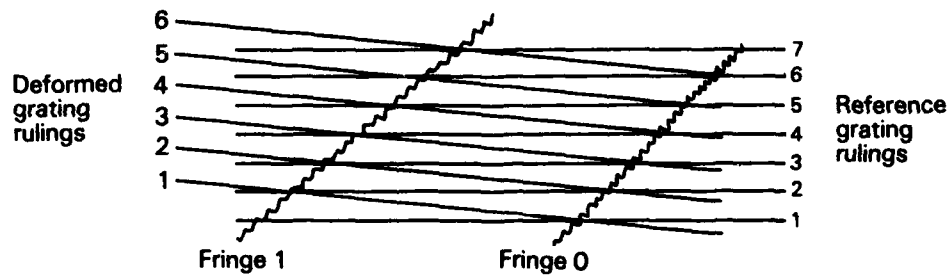


FIG 1: DIFFRACTION GRATING ACTION



Relative conditions between the gratings are identical along fringes 0 and 1.

Points of the deformed grating along fringe 1 have moved normal to the reference grating rulings by one pitch of the reference grating, relative to points along fringe 0.

FIG 2: MOIRE FRINGE INTERPRETATION

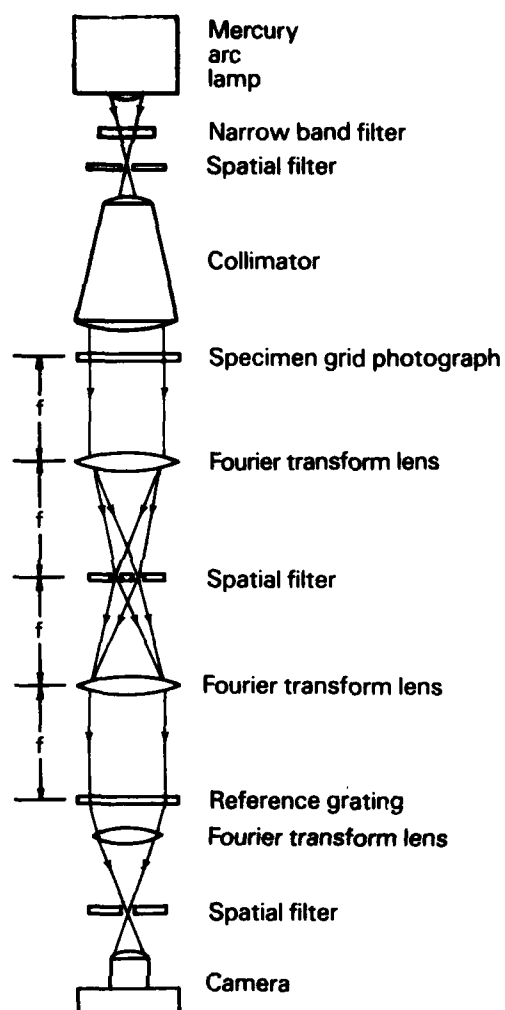


FIG 3: MOIRE OPTICAL PROCESSOR

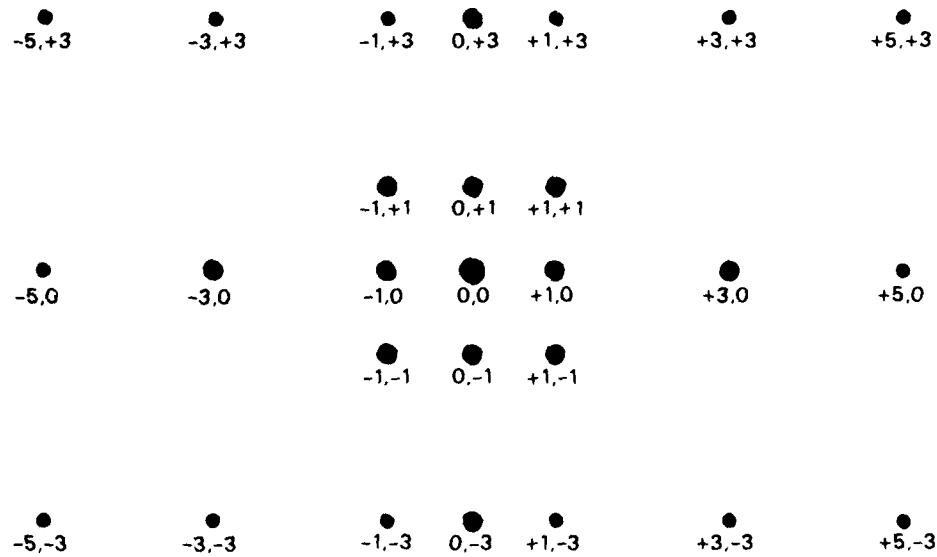


FIG 4: PICTORIAL NEGATIVE OF RONCHI GRID TRANSFORM

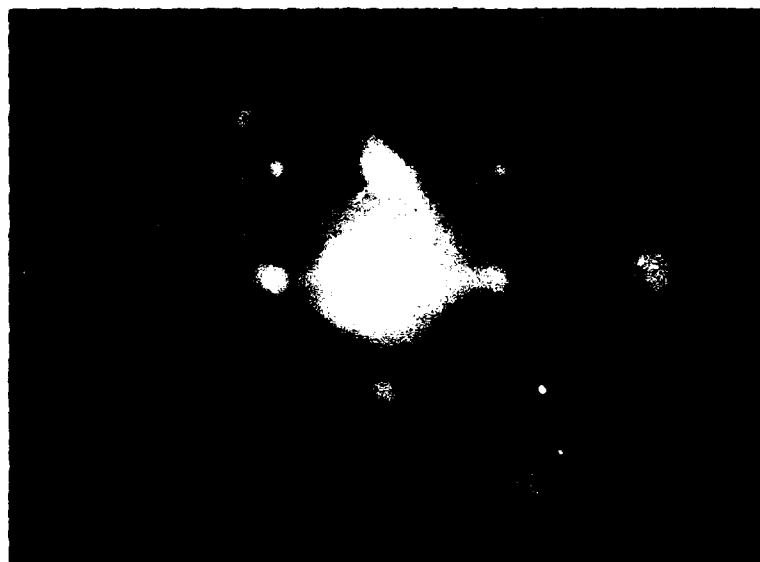


FIG 5: TYPICAL SPECIMEN GRID TRANSFORM



Technical drawing of a mechanical part, showing front and side views with dimensions.

**Front View Dimensions:**

- Overall length: 152.4
- Distance from left face to center of first hole: 76.2
- Hole diameters: 15.9 Dia (left and right), 8.37 Dia before cold working (center)
- Distance from left face to center of first hole: 19
- Distance from center of first hole to center of second hole: 41.3
- Distance from center of second hole to center of third hole: 41.3
- Distance from center of third hole to right face: 19
- Overall width: 22.2
- Distance from top face to center of holes: 44.5

**Side View Dimensions:**

- Overall width: 8.89
- Distance from left face to center of first hole: 5.07

**All dimensions in millimetres**

**FIG 7: THE COLD-WORKED BOLT HOLE SPECIMEN**

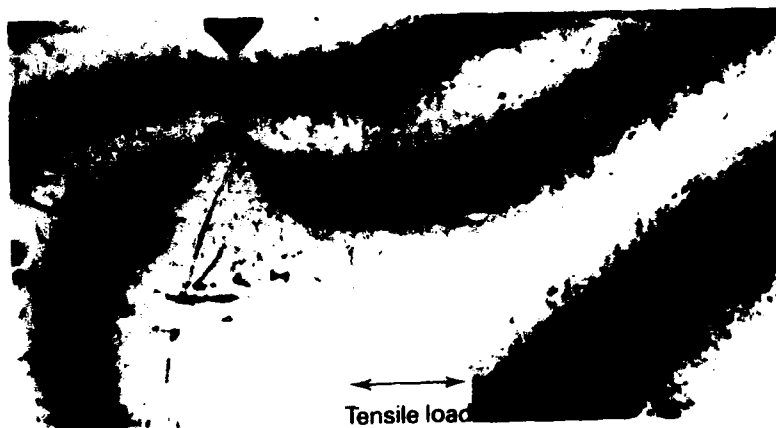


(a) Horizontal displacement

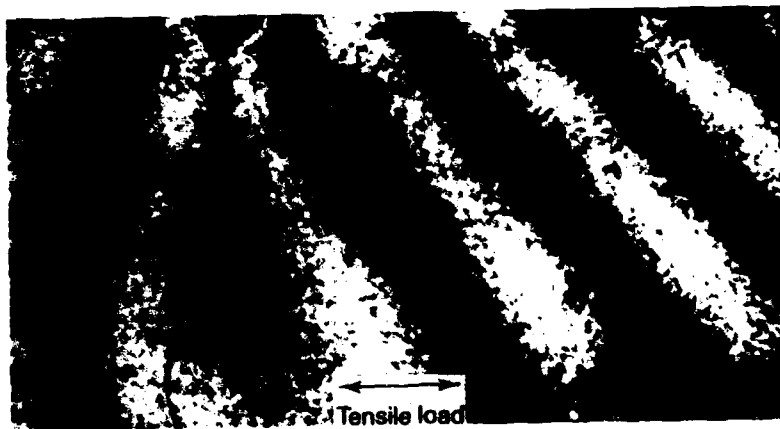


(b) Vertical displacement

FIG 8: J-INTEGRAL SPECIMEN CRACK REGION BEFORE LOADING



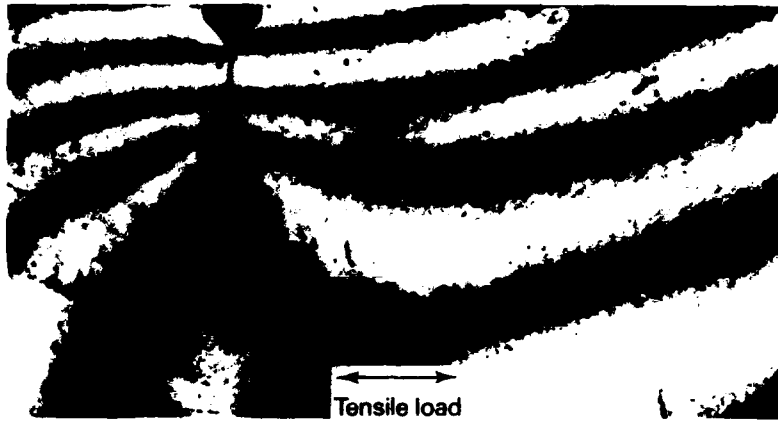
(a) Horizontal displacement



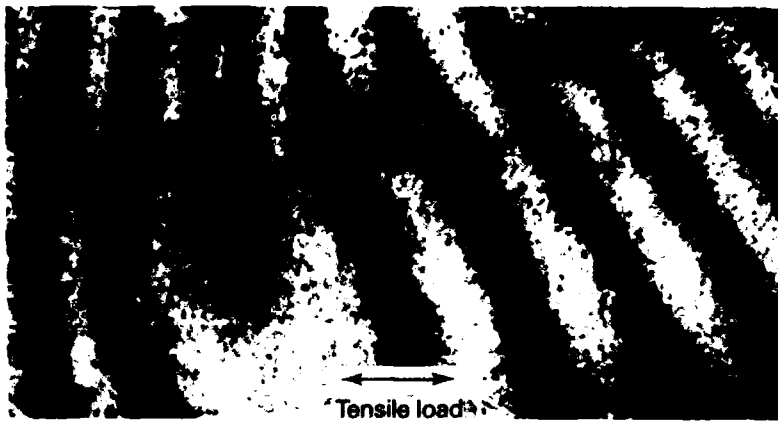
(b) Vertical displacement

FIG 9: J-INTEGRAL SPECIMEN CRACK REGION AT 1.06 kN



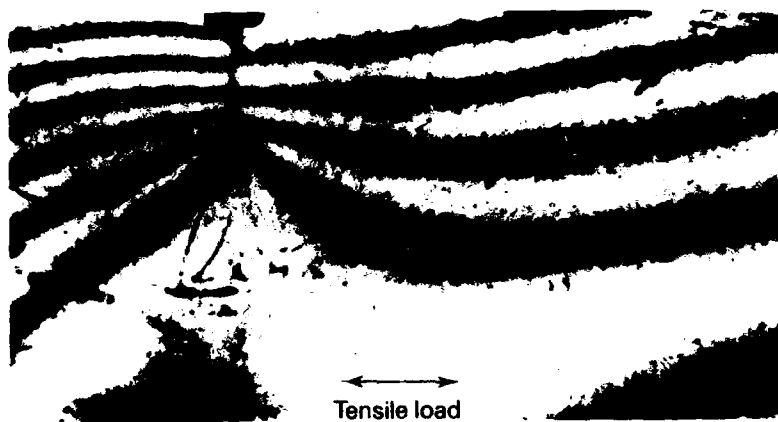


(a) Horizontal displacement

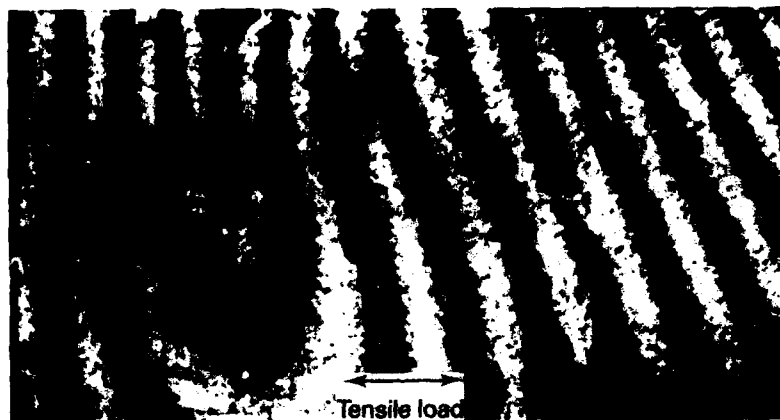


(b) Vertical displacement

FIG 10: J-INTEGRAL SPECIMEN CRACK REGION AT 2.11 kN



(a) Horizontal displacement



(b) Vertical displacement

FIG 11: J-INTEGRAL SPECIMEN CRACK REGION AT 3.17 kN



(a) Horizontal displacement



(b) Vertical displacement

FIG 12: J-INTEGRAL SPECIMEN CRACK REGION AFTER LOADING.

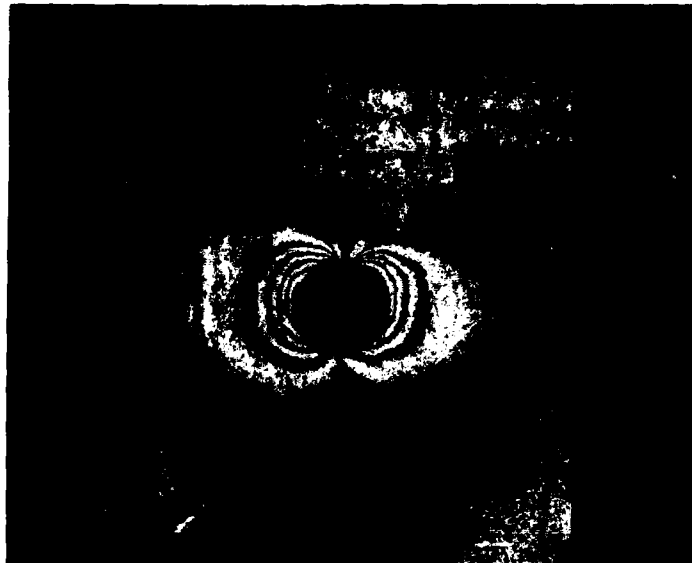


(a) Horizontal displacement



(b) Vertical displacement

FIG 13: COLD-WORKED BOLT HOLE SPECIMEN FRONT FACE AT MAXIMUM EXPANSION



(a) Horizontal displacement



(b) Vertical displacement

FIG 14: COLD-WORKED BOLT HOLE SPECIMEN FRONT FACE AFTER COLD WORKING



(a) Horizontal displacement

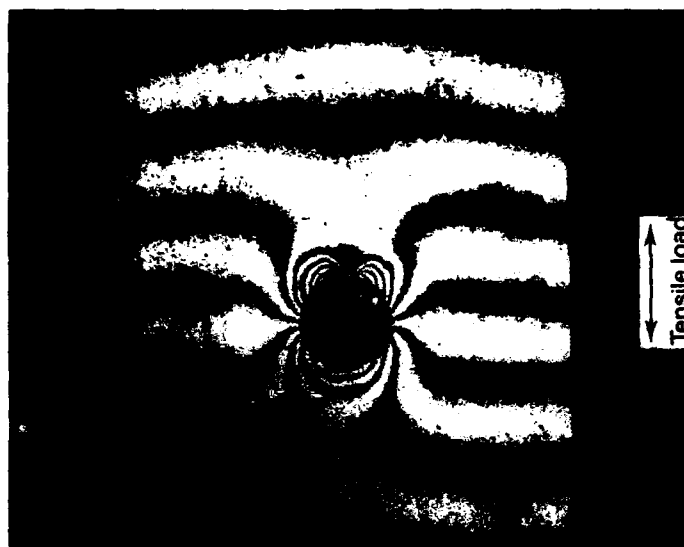


(b) Vertical displacement

FIG 15: COLD-WORKED BOLT HOLE SPECIMEN BACK FACE AFTER COLD WORKING



(a) Horizontal displacement



(b) Vertical displacement

FIG 16: COLD-WORKED BOLT HOLE SPECIMEN FRONT FACE AT 47.8 kN AFTER COLD WORKING



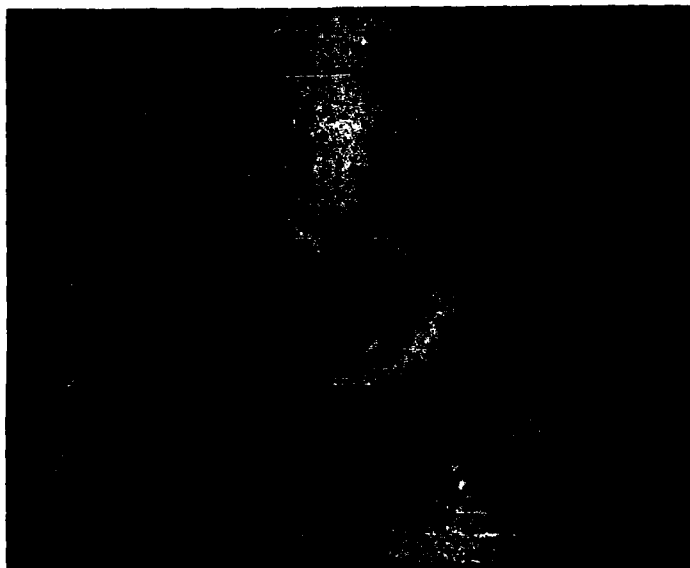
(a) Horizontal displacement



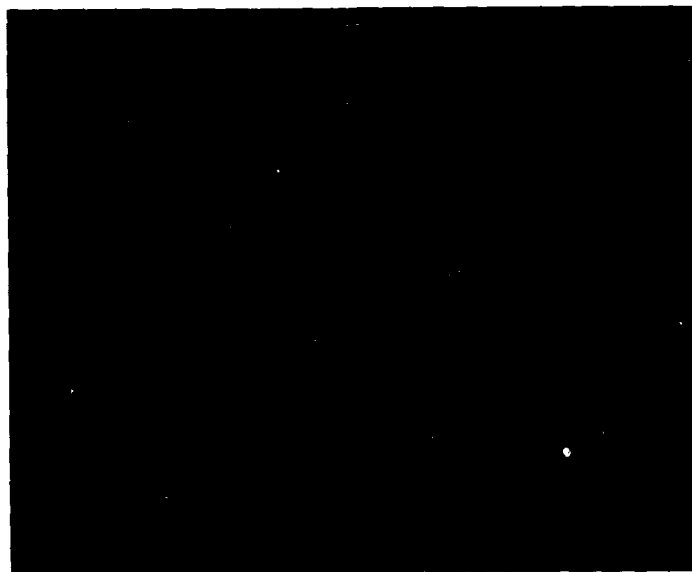
(b) Vertical displacement

FIG 17: COLD-WORKED BOLT HOLE SPECIMEN BACK FACE AT 47.8 kN AFTER COLD WORKING





(a) Horizontal displacement

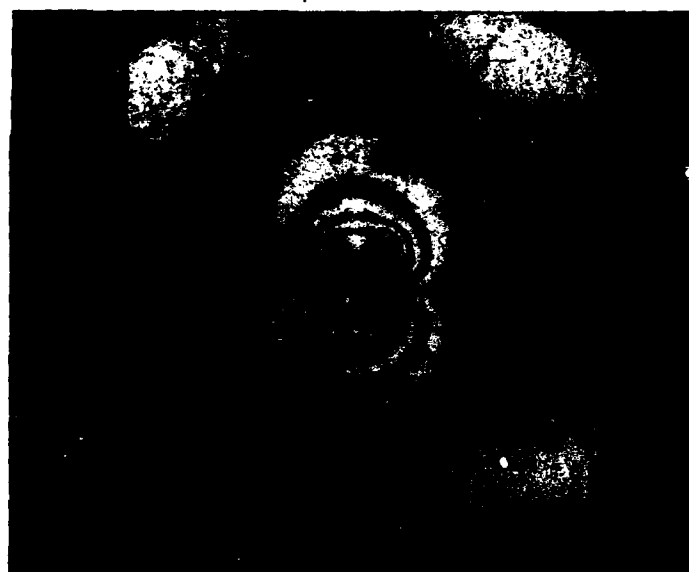


(b) Vertical displacement

FIG 18: COLD-WORKED BOLT HOLE SPECIMEN FRONT FACE AFTER COLD WORKING AND LOADING



(a) Horizontal displacement



(b) Vertical displacement

FIG 19: COLD-WORKED BOLT HOLE SPECIMEN BACK FACE AFTER COLD WORKING AND LOADING

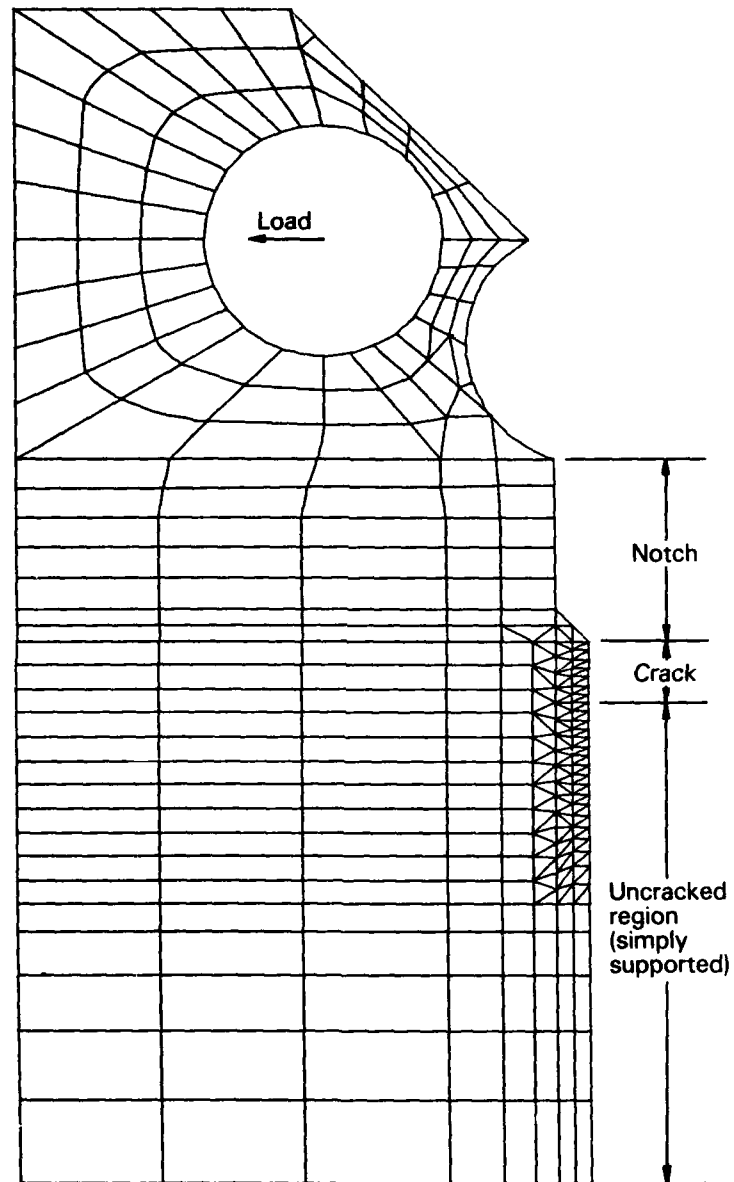


FIG 20: J-INTEGRAL SPECIMEN FE MESH

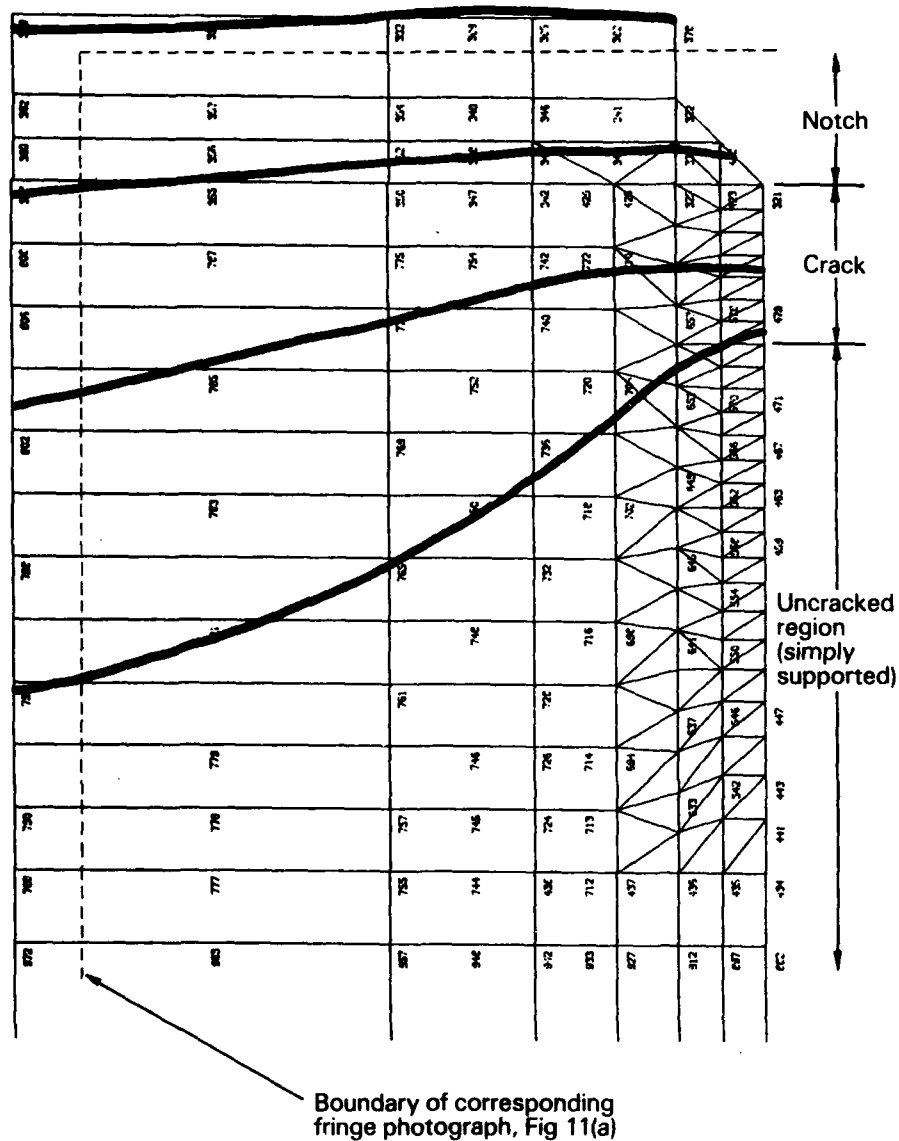


FIG. 21: HORIZONTAL DISPLACEMENT CONTOURS - CRACK REGION OF J-INTEGRAL SPECIMEN AT 3.17 kN

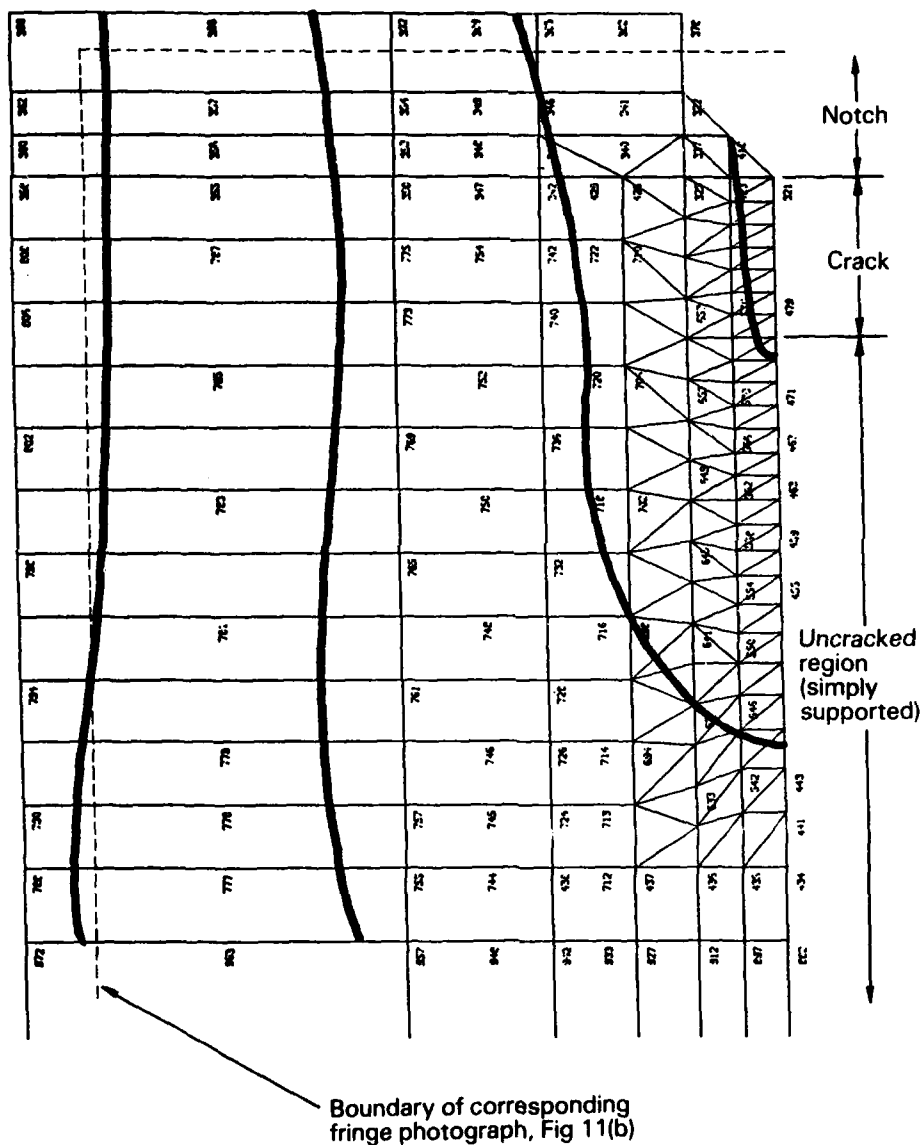


FIG. 22: VERTICAL DISPLACEMENT CONTOURS - CRACK REGION OF J-INTEGRAL SPECIMEN AT 3.17 kN

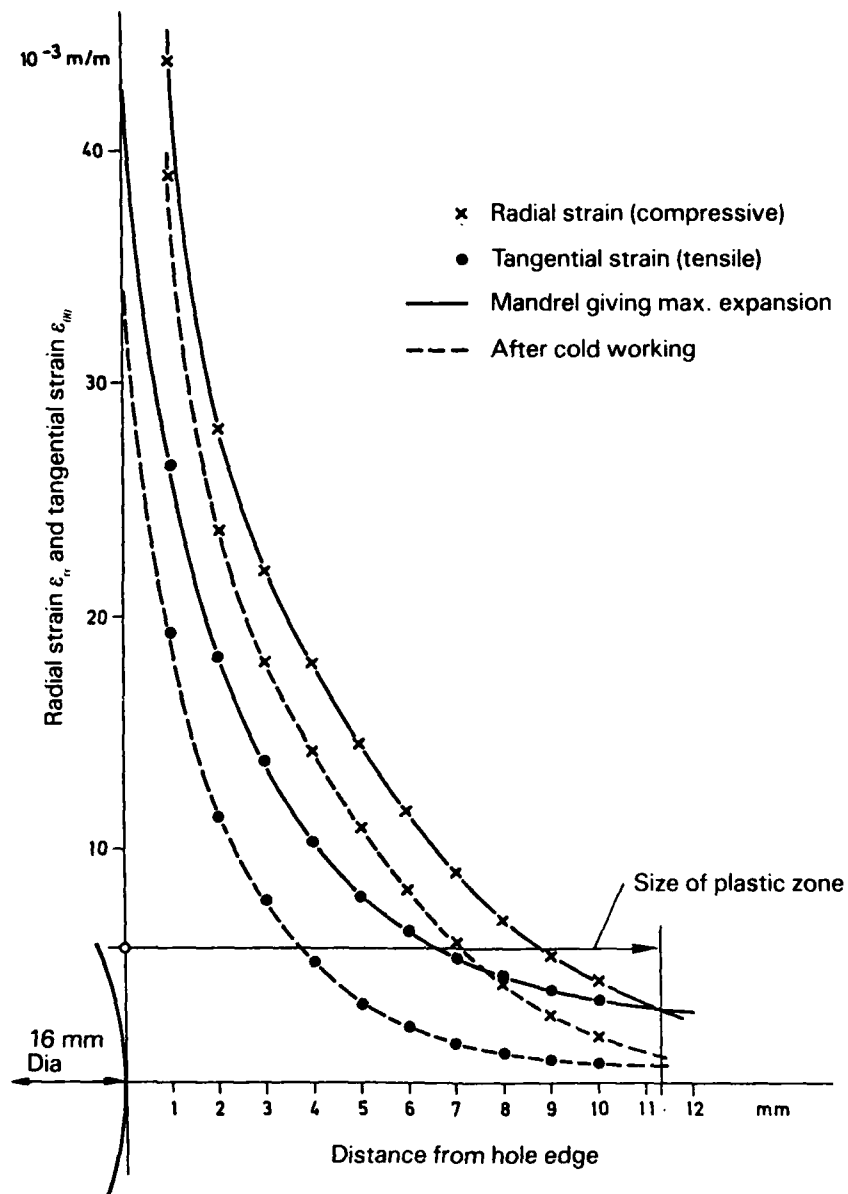
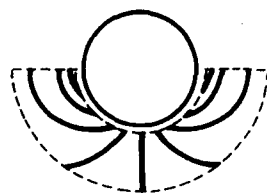
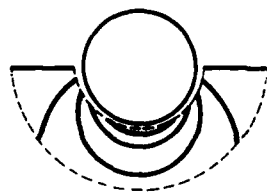


FIG 23: STRAINS FROM COLD WORKING

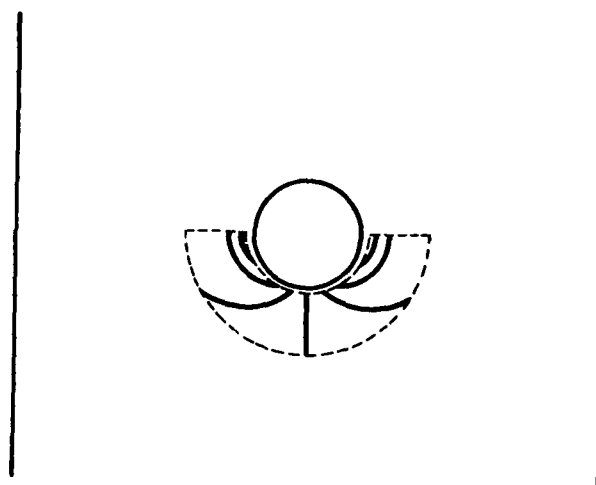


(a) Horizontal displacement

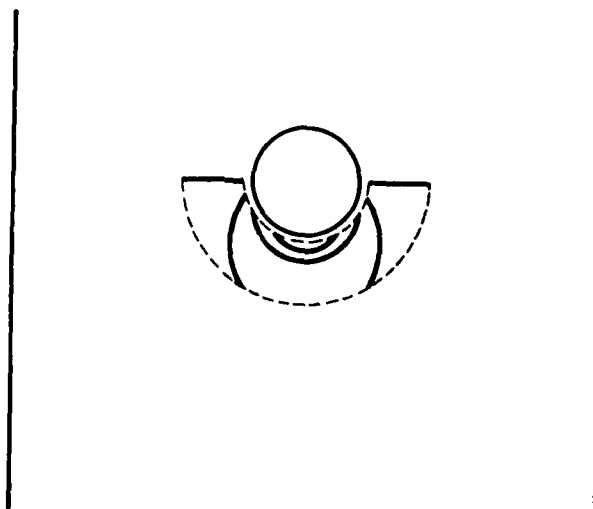


(b) Vertical displacement

FIG 24: DISPLACEMENT CONTOURS AT MAXIMUM EXPANSION FROM COLD WORKING



(a) Horizontal displacement



(b) Vertical displacement

FIG 25: DISPLACEMENT CONTOURS AFTER COLD WORKING



## **DISTRIBUTION**

### **AUSTRALIA**

#### **Department of Defence**

##### **Defence Central**

Chief Defence Scientist  
Deputy Chief Defence Scientist (shared copy)  
Superintendent, Science and Program Administration (shared copy)  
Controller, External Relations, Projects and  
Analytical Studies (shared copy)  
Director, Departmental Publications  
Counsellor, Defence Science (London) (Doc Data sheet only)  
Counsellor, Defence Science (Washington) (Doc Data sheet only)  
SA to the Thailand Military R and D Centre (Doc Data sheet only)  
SA to the D R C (Kuala Lumpur) (Doc Data sheet only)  
OIC TRS, Defence Central Library  
Document Exchange Centre, DISB (18 copies)  
Joint Intelligence Organisation  
Librarian H Block, Victoria Barracks, Melbourne  
Director General — Army Development (NSO) (4 copies)  
Defence Industry and Materiel Policy, FAS

##### **Aeronautical Research Laboratories**

Director  
Library  
Divisional File — Structures  
Author: K. C. Watters  
B. Lawrie  
R. Jones  
S. Rumble  
J.G. Sparrow  
A. Wong

##### **Materials Research Laboratories**

Director/Library

##### **Defence Research Centre**

Library

##### **RAN Research Laboratory**

Library

**Navy Office**

Navy Scientific Adviser (Doc Data sheet only)  
Director of Naval Aircraft Engineering

**Army Office**

Scientific Adviser — Army (Doc Data sheet only)  
Engineering Development Establishment, Library  
Royal Military College Library

**Air Force Office**

Air Force Scientific Adviser (Doc Data sheet only)  
Aircraft Research and Development Unit  
Scientific Flight Group  
Library  
Technical Division Library  
Director General Aircraft Engineering — Air Force  
RAAF College, Point Cook

**Central Studies Establishment**

Information Centre

**Aerospace Technologies Australia**

Manager  
Librarian

**Department of Aviation**

Library

**Statutory and State Authorities and Industry**

Australian Nuclear Science & Technology Organisation  
Commonwealth Aircraft Corporation, Library  
Hawker de Havilland Aust Pty Ltd, Bankstown, Library  
Hawker de Havilland Aust Pty Ltd, Victoria, Library  
CSIRO, Applied Physics Division  
Dr P. Hariharan  
Dr B. Oreb  
CSIRO, Chemical Physics Division  
Dr I. Wilson

#### **Universities and Colleges**

Adelaide	Barr Smith Library
Flinders	Library
La Trobe	Library
Melbourne	Engineering Library
Monash	Hargrave Library
Newcastle	Library
New England	Library
Sydney	Engineering Library
NSW	Physical Sciences Library Library, Australian Defence Force Academy
Queensland	Library
Tasmania	Engineering Library
Western Australia	Library
RMIT	Library

#### **CANADA**

CAARC Coordinator Structures

NRC

Aeronautical & Mechanical Engineering Library

#### **Universities and Colleges**

Toronto

Institute for Aerospace Studies

#### **INDIA**

CAARC Coordinator Structures  
National Aeronautical Laboratory, Information Centre

#### **JAPAN**

National Aerospace Laboratory  
Institute of Space and Aeronautical Science, Library

#### **NETHERLANDS**

National Aerospace Laboratory (NLR), Library

#### **NEW ZEALAND**

Defence Scientific Establishment, Library

#### **SWEDEN**

Aeronautical Research Institute, Library

#### **SWITZERLAND**

F+W (Swiss Federal Aircraft Factory)

#### **UNITED KINGDOM**

Royal Aircraft Establishment  
Bedford, Library  
Farnborough, Dr. G. Wood, Materials Department  
National Physical Laboratory, Library  
National Engineering Laboratory, Library  
CAARC Co-ordinator, Structures  
Rolls-Royce Ltd, Aero Division Bristol, Library

#### **Universities**

London  
Professor G.J. Hancock, Aero Engineering

Cranfield Inst. of Technology  
Library

Imperial College  
Aeronautics Library

**UNITED STATES OF AMERICA**

**NASA Scientific and Technical Information Facility**

**Universities and Colleges**

**Virginia Polytechnic Institute and State University**

**Professor D. Post**

**(Blacksburg, VA 24061)**

**SPARES (10 copies)**

**TOTAL (107 copies)**

AL 148  
REVISED APRIL 87

DEPARTMENT OF DEFENCE

DOCUMENT CONTROL DATA

PAGE CLASSIFICATION  
UNCLASSIFIED

PRIVACY MARKING

1a. AIR NUMBER AR-004-543	1b. ESTABLISHMENT NUMBER ARL-STRUC-R-428	2. DOCUMENT DATE JULY 1987	3. TASK NUMBER DST 83/006
4. TITLE IN-PLANE MOIRE OPTICAL PROCESSING AT ARL		5. SECURITY CLASSIFICATION (PLACE APPROPRIATE CLASSIFICATION IN BOX (S) IE. SECRET (S), CONFIDENTIAL (C), RESTRICTED (R), UNCLASSIFIED (U).)	
		6. No. PAGES 37	
8. AUTHOR(S) K.C. WATTERS		7. No. REFS. 17	
9. DOWNGRADING/DECLASSIFYING INSTRUCTIONS		10. CORPORATE AUTHOR AND ADDRESS  AERONAUTICAL RESEARCH LABORATORIES P.O. BOX 4331, MELBOURNE VIC. 3001	
11. OFFICE/POSITION RESPONSIBLE FOR SPONSOR ----- SECURITY ----- DOWNGRADING ----- APPROVAL -----		12. SECONDARY DISTRIBUTION (OF THIS DOCUMENT) Approved for Public Release	
OVERSEAS ENQUIRIES OUTSIDE STATED LIMITATIONS SHOULD BE REFERRED THROUGH ASDIS, DEFENCE INFORMATION SERVICES BRANCH, DEPARTMENT OF DEFENCE, CAMPBELL PARK, CANBERRA, ACT 2601			
13a. THIS DOCUMENT MAY BE ANNOUNCED IN CATALOGUES AND AWARENESS SERVICES AVAILABLE TO..... No limitations			
13b. CITATION FOR OTHER PURPOSES (IE. CASUAL ANNOUNCEMENT) MAY BE <input checked="" type="checkbox"/> UNRESTRICTED OR <input type="checkbox"/> AS FOR 13a.			
14. DESCRIPTIONS Moire fringe methods, <i>Strain Measurement</i> Optical interferometers, <i>Aust. a/c [unclear]</i>		15. ORDA SUBJECT CATEGORIES 0046C 0094J 0071L	
16. ABSTRACT The principle and operation of the <i>ARL</i> in-plane moire optical processor are described in detail. The processor uses extensive spatial filtering to produce dual-beam interference moire fringes of high contrast. Fringe patterns obtained from a J-integral specimen and a cold-worked bolt hole specimen are shown. They compare well with displacement contour patterns obtained from a theoretical analysis and strain gauge data. <i>keywords:</i>			

PAGE CLASSIFICATION

PRIVACY MARKING

THIS PAGE IS TO BE USED TO RECORD INFORMATION WHICH IS REQUIRED BY THE ESTABLISHMENT FOR ITS OWN USE BUT WHICH WILL NOT BE ADDED TO THE DISTIS DATA UNLESS SPECIFICALLY REQUESTED.

16. ABSTRACT (CONT.)

17. IMPRINT

AERONAUTICAL RESEARCH LABORATORIES, MELBOURNE

18. DOCUMENT SERIES AND NUMBER

Structures Report 428

19. COST CODE

271055

20. TYPE OF REPORT AND PERIOD COVERED

21. COMPUTER PROGRAMS USED

22. ESTABLISHMENT FILE REF. (S)

23. ADDITIONAL INFORMATION (AS REQUIRED)